

# COVER SHEET

## Assessing Decadal Variability of Subseasonal Forecasts of Opportunity using Explainable AI

Marybeth Arcodia<sup>1</sup>, Elizabeth A. Barnes<sup>1</sup>, Kirsten Mayer<sup>1,2</sup>, Jiwoo Lee<sup>3</sup>, Ana Ordonez<sup>3</sup>,  
Min-Seop Ahn<sup>3,4,5</sup>

<sup>1</sup> Colorado State University, Fort Collins CO, USA

<sup>2</sup> National Center for Atmospheric Research, Boulder CO, USA

<sup>3</sup> Lawrence Livermore National Laboratory, Livermore, CA, USA

<sup>4</sup> NASA Goddard Space Flight Center, Greenbelt, MD, USA

<sup>5</sup> ESSIC, University of Maryland, College Park, MD, USA

Corresponding author email: [marcodia@rams.colostate.edu](mailto:marcodia@rams.colostate.edu)

Corresponding author Twitter: @mbarcodia

*This is a non-peer reviewed preprint submitted to EarthArXiv. This manuscript is currently submitted to Environmental Research: Climate.*

# Assessing Decadal Variability of Subseasonal Forecasts of Opportunity using Explainable AI

Marybeth Arcodia<sup>1</sup>, Elizabeth A. Barnes<sup>1</sup>, Kirsten Mayer<sup>1,2</sup>, Jiwoo Lee<sup>3</sup>, Ana Ordonez<sup>3</sup>,  
Min-Seop Ahn<sup>3,4,5</sup>

<sup>1</sup> Colorado State University, Fort Collins CO, USA

<sup>2</sup> National Center for Atmospheric Research, Boulder CO, USA

<sup>3</sup> Lawrence Livermore National Laboratory, Livermore, CA, USA

<sup>4</sup> NASA Goddard Space Flight Center, Greenbelt, MD, USA

<sup>5</sup> ESSIC, University of Maryland, College Park, MD, USA

Corresponding author email: [marcodia@rams.colostate.edu](mailto:marcodia@rams.colostate.edu)

## Abstract

Identifying predictable states of the climate system allows for enhanced prediction skill on the generally low-skill subseasonal timescale via forecasts with higher confidence and accuracy, known as forecasts of opportunity. This study takes a neural network approach to explore decadal variability of subseasonal predictability, particularly during forecasts of opportunity. Specifically, this work quantifies subseasonal prediction skill provided by the tropics within the CESM2 Large Ensemble and assesses how this skill evolves on decadal timescales. Utilizing the networks' confidence and explainable artificial intelligence (XAI), physically meaningful sources of predictability associated with periods of enhanced skill are identified. Using these networks, we find that tropically-driven subseasonal predictability varies on decadal timescales during forecasts of opportunity. Analysis is extended to ECMWF Reanalysis v5 data, revealing that the relationships learned within the CESM2-LE holds in modern reanalysis data. These results indicate that the neural networks are capable of identifying predictable decadal states of the climate system within CESM2 that are useful for making confident, accurate subseasonal precipitation predictions in the real world.

Keywords: forecasts of opportunity, subseasonal predictability, explainable machine learning, decadal variability

## 1. Introduction

The subseasonal timescale, ranging from approximately 2 weeks to 3 months, is often described as a “desert of predictability” due to its lack of forecast skill (Vitart et al., 2017). Despite this issue, there is heightened demand from local management officials, water managers, and stakeholders for forecasts beyond the weather timescale to allow for longer lead times for preparation (Mariotti et al., 2019; NASEM 2016; Vitart et al., 2017). This has led to increased efforts to understand subseasonal phenomena and the large-scale features that modulate them, in order to improve predictability. Subseasonal predictability stems from knowledge of initial and boundary conditions that capture the coupled interactions which constrain chaotic processes in the atmosphere (Lovejoy, 2018; Vitart, 2017). Forecasters rely on predictable states of the climate system that can lead to periods of higher prediction skill within the subseasonal timescale, e.g. *forecasts of opportunity*, to improve subseasonal forecasts (Albers & Newman, 2019; Mariotti et al., 2020). These forecasts can be made by strategically leveraging time periods when certain large-scale oceanic and atmospheric conditions that provide sources of subseasonal predictability are present.

Efforts to recognize when and where forecasts of opportunity will occur often focus on identifying climate processes that lead to enhanced prediction skill and/or predictability. The tropics have been identified as a key source of midlatitude predictability via tropical-extratropical teleconnections (Hoskins & Karoly, 1981; W. K. M. Lau et al., 2012; Matthews et al., 2004; Pegion & Kirtman, 2008). For example, the Madden-Julian Oscillation (MJO; (Madden & Julian, 1971)) is the dominant mode of tropical intraseasonal variability, known to influence circulation and precipitation changes around the globe (Cassou, 2008; Jones & Carvalho, 2012; Ling et al., 2017; Stan et al., 2017; Zhang, 2005, 2013). Specifically, midlatitude subseasonal variability linked to the MJO affects precipitation in Alaska (Zheng et al. 2018), the Pacific-Northwest (Bond and Vecchi 2003), and California (Arcodia et al. 2020). Additionally, MJO teleconnections in the United States can be modulated by lower frequency modes such as ENSO (Arcodia & Kirtman, 2022; Moon et al., 2011; Tseng et al., 2020). When active, the combined influence of the MJO and ENSO conditions can provide subseasonal forecasts of opportunity for

midlatitude precipitation (Arcodia et al., 2020; DeFlorio et al., 2019; Johnson et al., 2014; Newman et al., 2003).

Seasonal-to-interannual variability, such as ENSO, and its impact on subseasonal predictability has also been explored in recent years (Huang et al., 2021; R. W. Lee et al., 2019), however, lower frequency modes of variability on decadal timescales and its impact on subseasonal predictability is much less studied. Some previous work has explored how decadal variability influences seasonal midlatitude precipitation variability (Cayan et al. 1998; Gershunov and Barnett 1998; McCabe and Dettinger 1999; Dai 2013). In addition, prior efforts have identified decadal modulation of MJO teleconnections (Kim 2020) and low frequency variability in subseasonal predictability of the North Atlantic Oscillation (Albers & Newman, 2021; Luo et al., 2022; O'Reilly et al., 2017; Scaife et al., 2014; Weisheimer et al., 2017). However, this raises the question as to whether there is a subsequent impact of decadal variability on midlatitude subseasonal predictability provided by the tropics.

Recent improvements to subseasonal forecast skill have been attributed to identifying forecasts of opportunity based on improved initial conditions and active climate modes in official forecasting systems (Mariotti et al., 2020). Additionally, improvements to forecasting models have enhanced subseasonal prediction skill, which can be attributed to higher resolution and better physical parameterizations (Meehl et al., 2021; Pegion et al., 2019). Here, we seek to explore the role of decadal variability on regional subseasonal prediction skill in the recent decades. It is important to identify and better understand the impact of decadal variability on subseasonal predictability, as this variability could affect the performance of these models in the future. Unfortunately, this investigation remains a challenging task due to the lack of historical data and historical hindcasts needed to assess variability of subseasonal predictability on decadal timescales.

To combat this issue, we utilize the Community Earth System Model Version 2 - Large Ensemble (CESM2-LE; (Danabasoglu et al., 2020)) to analyze 1,000 years of climate model data. Specifically, we use the CESM2 historical simulation to train neural networks to quantify the subseasonal prediction skill within CESM2 without the need for a forecast model. The fields of weather and climate science have benefitted from applications of neural networks to learn physical relationships within the Earth system via explainability techniques (Gordon et al., 2021; Ham et al., 2019; Mamalakis et al., 2021; Martin et al., 2022; Mayer & Barnes, 2022; McGovern et al., 2019; Toms et al., 2020; van Straaten et al., 2023). Here, we use shallow artificial neural networks to quantify U.S. West Coast subseasonal precipitation skill and identify forecasts of opportunity provided by the tropics within CESM2. We assess the low frequency

variability of the subseasonal prediction skill, finding decadal variability in skill particularly during forecasts of opportunity. ERA5 data are then input into the neural networks to make predictions based only on learned CESM2 relationships. The ERA5 results show skill above random chance, with enhanced skill for the forecasts of opportunity that oscillate on decadal timescales throughout the modern era.

## **2. Data and Methods**

### **2a. Climate Model Data**

Training artificial neural networks to learn predictive subseasonal signals amongst noisy climate data is a data-intensive process (Rosa et al., 2020). Thus, we take advantage of historical simulations performed as part of the CESM-2 Large Ensemble (CESM2-LE; (Danabasoglu et al., 2020)). Specifically, we analyze ten members which were selected to sample the four pre-selected initial states for different AMOC states and include smoothed biomass burning (SMBB). Results were ultimately not sensitive to the initialized AMOC state (not shown) and so the ten members should be generally viewed as ten largely independent realizations of the same historical climate. We found ten ensemble members to be sufficient, which is consistent with Mayer and Barnes (2021) who found ten members sufficient for a similar problem. Additional information about the ensemble members used can be found in the Supplemental Table 1.

Daily precipitation data are interpolated to 2.5 by 2.5 degree resolution and selected from 1850-1949. We use data from November-March since boreal winter is known to have strong tropical-extratropical teleconnections in the Northern Hemisphere (Soulard et al., 2021; Weickmann, 1983). Daily precipitation anomalies are calculated by subtracting the linear trend of the ensemble mean for each day of year from each grid point independently to retain only internal variability. Similar analyses were performed using the pre-industrial control runs which yielded comparable behavior (not shown), confirming the effective removal of the forced response.

We train a set of artificial neural networks (more details provided in Section 2c) to ingest a map of daily tropical precipitation anomalies and classify the sign (i.e. positive or negative) of the midlatitude subseasonal precipitation anomaly (Fig. 1). The inputs (predictors) to the neural network are maps of the daily tropical precipitation anomalies from 26°S to 26°N where each grid point represents an individual node in the input layer. The outputs (predictands) are the sign of precipitation averaged over days 22-35

(Week 4-5) after the input day. For example, the input map for November 1, 1850 is used to predict the sign of the averaged November 23-December 6, 1850 precipitation anomaly in the three predicted regions. Next, the input map for November 2, 1850 is used to predict the sign of the November 24-December 7, 1850 anomaly, and so on. The output data is area-averaged over coastal Alaska (58.75-63.75°N; 202.5-220°E), the Pacific Northwest (41.25-48.75°N; 235-242.5°E), and California (33.75-41.25°N; 235-242.5°E) as shown in Figure 1.

Ten sets of experiments are conducted. For each experiment, ten neural networks are trained on 8 ensemble members (the training set) with 100 years of data each, and each of the ten networks is initialized with a different random seed to sample uncertainty in the network initialization and ensure robustness of the results. Each trained neural network is then validated on one of the remaining members and tested on the other. The training, validation, and testing members are then reorganized so a new set of eight members are used to train the ten neural networks (each initialized with ten random seeds) that are validated on one member, and tested on the remaining member. This process is repeated 10 times, so that each ensemble member is used as a test member. With ten random initializations per network, this results in a set of 100 trained neural networks.

Prior to training the neural networks, the input data are normalized by subtracting the mean and dividing by the standard deviation of each grid point across the training/validation data. As a note, the daily anomalies are calculated with the training and validation members used for each set of neural networks to ensure that no information about the testing data is given to the neural networks during training. The output data is normalized by removing the median of the training/validation output data, then converted to binary to represent the sign of the anomalies (0s for a negative prediction; 1 for a positive prediction). The training and the validation output data are class balanced by randomly removing samples so that there are equal numbers of 0s and 1s.

## 2b. Reanalysis Data

We also use precipitation from the ECMWF Reanalysis v5 (ERA5; (Hersbach et al., 2020)) dataset to evaluate the neural networks trained on the CESM2-LE. We interpolate the precipitation fields to 2.5 by 2.5 degree resolution and use November-March. However, due to data availability, we take the 00:00 time step at each grid point and our ERA5 analysis spans a later time period: 1959-2021. The trend is calculated by fitting a 3rd order polynomial to each day of year to capture any climate change signal, particularly in recent history. The ERA5 daily precipitation anomalies are then calculated via subtraction

of the trend. While removing the trend here does not capture the true forced response as was done with the CESM2 ensemble mean, removing the trend is sufficient for removing the forced response for a reanalysis dataset where multiple ensemble members are not available. Prior to inputting the ERA5 fields to the trained network, the data are normalized by subtracting the mean of the ERA5 data and dividing by the standard deviation of the ERA5 data at each grid point. This is done to ensure that the reanalysis and CESM2 data are in data-relative units prior to being input into the neural network. The standardized ERA5 data are converted to binary labels after the median is removed.

## 2c. Neural Network Architecture

The artificial neural network (ANN) architecture is depicted in Figure 1. The ANN consists of two hidden layers, the first with 128 nodes and the second with 32 nodes, both of which use a rectified linear activation function (ReLU). The final output layer consists of two nodes, representing our two classes: a negative or positive sign. This final layer uses the softmax function so that the two output values sum to one and thus represent an estimation of probability. This probability is then used to choose the predicted output, where the output with a probability greater than 0.5 is chosen as the selected class. This probability is also deemed our “network confidence” following the methodology of Mayer and Barnes (2021, 2022).

The network is trained using a categorical cross-entropy loss function with a batch size of 512 samples, a ridge regression coefficient of 5.0 (to minimize overfitting), and a learning rate of  $6.7e-6$ . Early stopping is also applied if validation loss does not decrease after 25 epochs. The 10 random seeds used are 210, 47, 33, 133, 410, 692, 64, 99, 910, 92. Hyperparameter tuning was performed using the KerasTuner (O’Malley et al., 2019) to find the optimal set of hyperparameters across all regions. The same set of hyperparameters is used for all 100 neural networks.

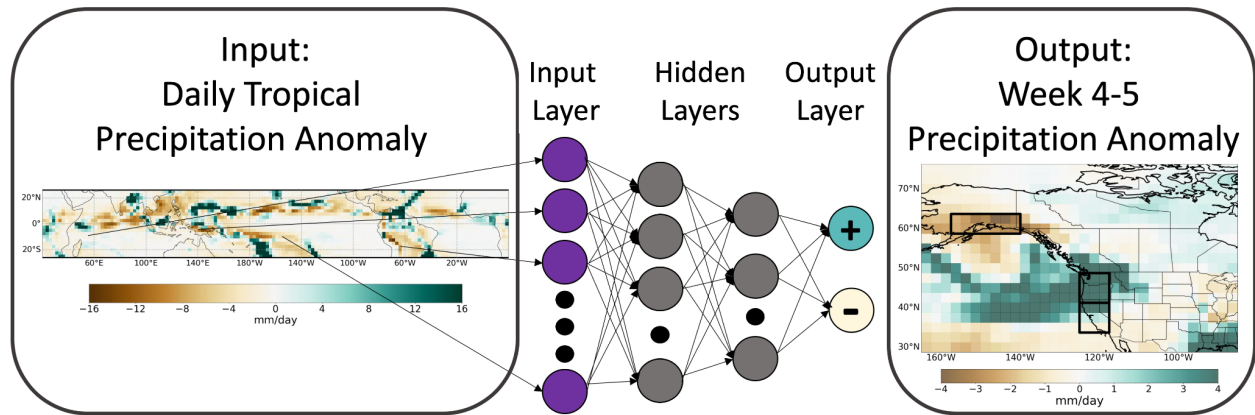


Fig 1. The artificial neural network input (daily tropical precipitation anomaly maps), the architecture consisting of 2 hidden layers with 128 nodes and 32 nodes respectively, and the output layer (sign of the Week 4-5 precipitation anomaly in the three boxed regions: Alaska, Pacific Northwest, and California).

## 2d. Explainable AI

Explainable artificial intelligence (XAI) methods have been utilized to open the “black box” of machine learning to gain insights about the climate system (Gordon et al., 2021; Labe & Barnes, 2022; Mamalakis et al., 2021, 2022; Mayer & Barnes, 2021; McGovern et al., 2019; Pegion et al., 2022; Sonnewald et al., 2021). Here, we use an XAI attribution method known as integrated gradients (Sundararajan et al., 2017). Integrated gradients is an extension of the Input\*Gradient method derived from the gradient/saliency method (Baehrens et al., 2010) which explains the network’s decision by computing the first partial derivative of the network’s output with respect to the input. An input has a high relevance value if the network used that feature to make its prediction. Integrated gradients is used here as it is a nonlinear version of the Input\*Gradient method and can identify properties of nonlinear relationships (Bommer et al., 2023).

An important choice when using integrated gradients is the baseline, from which all attributions are computed (Mamalakis et al., 2021). For this study, we choose a baseline input of zeros, since the daily anomalies are centered around zero by construction. We note that the corresponding network output for a zero input is roughly 50% probability for both classes, implying that our baseline for an input of all zeros is uninformative when it comes to precipitation prediction. This behavior is preferable for classification problems, and is intuitive for our problem in that zero anomalies (i.e. the mean) hold no predictive information (Mamalakis et al., 2023; Sundararajan et al., 2017).



## 3. Results

### 3a. Forecasts of Opportunity

The neural networks are designed to take a map of daily tropical precipitation anomalies as input and classify the sign of the Week 4-5 precipitation anomaly in a particular U.S. region. Here, we focus our results on three regions known to be influenced by tropical teleconnections on subseasonal timescales: Alaska, the Pacific Northwest, and California. For each experiment (identified by the member used for testing), 10 neural networks are initialized with different random seeds and the average test accuracy across the ten networks is computed and shown in Figure 2a (squares). The mean of the 10 averaged accuracies, i.e. the mean of all 100 trained neural networks, is also shown in Figure 2a (large, dark squares). These accuracies are compared to an *untrained* network in which the testing data was used to make predictions with neural networks that were initialized with random weights, but not trained. The accuracy of the untrained networks can then be compared to that of the trained networks to assess if the trained networks resulted in higher accuracy than the untrained networks or random chance. For each of our three regions, the average accuracy of the untrained networks (crosses) is approximately 50%, as expected. The average accuracy from the trained (squares) are distinctly higher than the average accuracy of the untrained networks, indicating that the neural networks exhibit higher prediction skill than random chance.

We leverage the network's confidence in each prediction to identify forecasts of opportunity. In Figure 2b-d, the confidence values associated with each prediction for one experiment per region are ranked by percentile, ranging from "All" (e.g. 100% of the predictions; left) to the top 10% (right). Shading indicates the accuracy versus confidence for each of the untrained networks initialized with a different random seed, with the darker line indicating the average of the random seeds.

For each region, the accuracy increases as confidence increases (Fig. 2b-d). This is particularly evident when compared against the accuracy as a function of confidence for the untrained networks (gray lines). The accuracy of the untrained networks remains fairly constant as confidence increases, with a slight increase in accuracy for the top 10% of predictions due to higher variance from a smaller sample size. Supplemental Figure S1 shows the same as Figure 2b-d but for all 10 experiments for each region. Since the accuracy of our trained neural networks increases as confidence increases, the most confident predictions are also those predictions with the highest accuracy, and thus, are evidence of forecasts of

opportunity. From here on out, we define forecasts of opportunity as the 20% most confident predictions, however, our conclusions are insensitive to different confidence intervals selected ( $\pm 10\%$ ). The accuracy of the forecasts of opportunity are plotted in Figure 2a as diamonds for the three predictand regions, with the average of the accuracies consistently higher for the forecasts of opportunity (diamonds) than the average accuracy for all predictions (squares).

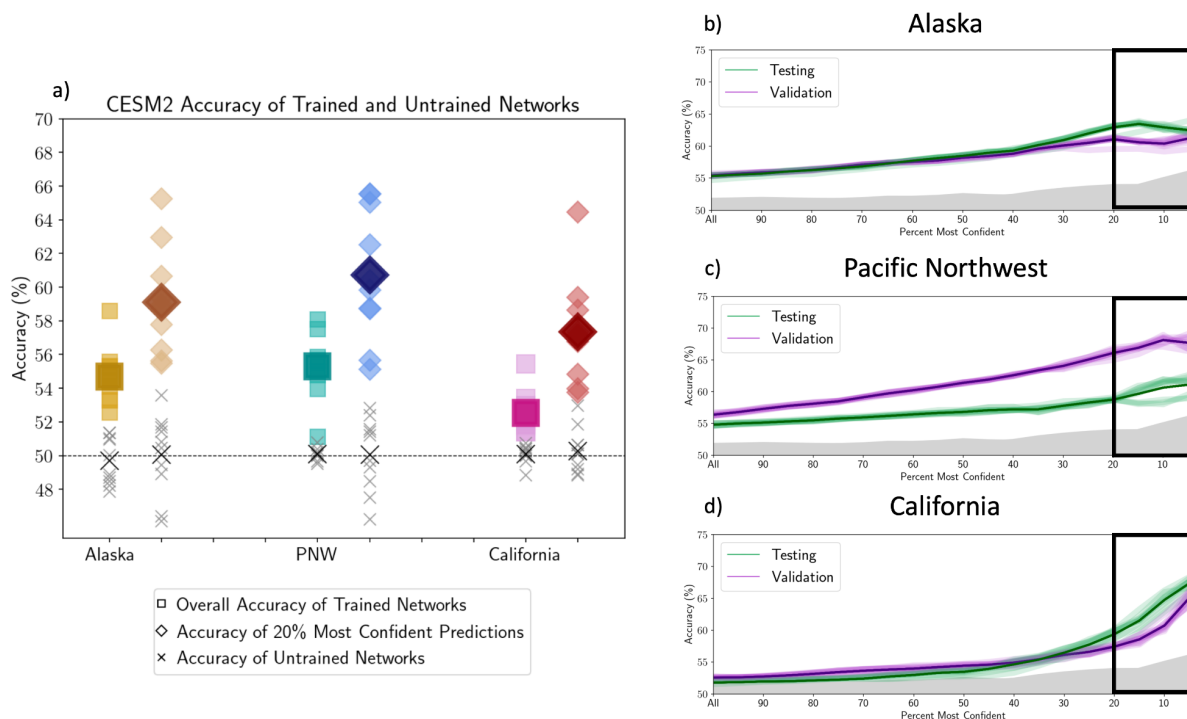


Fig 2. a) The average accuracy of testing data predictions for neural networks trained on CSM2 data from 1850-1949. Squares represent the average accuracy for 10 random seeds for all test ensemble members. Large, dark squares represent the average accuracy across all 100 networks. Gray “X”s represent the average accuracy of an untrained/random network with the dark X showing the average accuracy from the random network. b-d) The accuracy vs. confidence for b) Alaska, c) Pacific Northwest, and d) California for 10 random seeds for test ensemble member #0 of the testing data (light green lines) and the average accuracy of the testing data (dark green line), the 10 random seeds of the validation data (light purple lines) and average (dark purple line), and a random network (gray) with the gray box showing the region of predictions with the 20% most confidence for each region.

We then assess the output to determine if the sign of the predicted anomaly varies within a season, ensuring the networks were making subseasonal predictions, rather than seasonal predictions. A time series showing the subseasonal variability of the predictions is shown in Figure 3, in which the predictions vary between negative and positive within one season. We highlight forecasts of opportunity with darker/larger circles, showing that the network tends to be most confident in either a negative or

positive prediction for each season. For example, in the 1875-1876 winter the most confident predictions were all positive, but in the 1876-1877 winter, the confident predictions were all negative. Therefore, the networks demonstrate subseasonal variability in the anomaly sign prediction, but the most confident predictions are typically of the same sign within a season.

These results demonstrate that the neural networks perform better than random chance and can identify features in the input that makes the network more confident (and accurate) in its prediction. Next, we explore the sources of predictability the neural network is utilizing to make its confident and correct predictions in each region. We do this to ensure the neural network is identifying physically meaningful regions for subseasonal precipitation prediction along the West Coast of the U.S. before further exploring if the accuracy of these networks varies on decadal timescales.

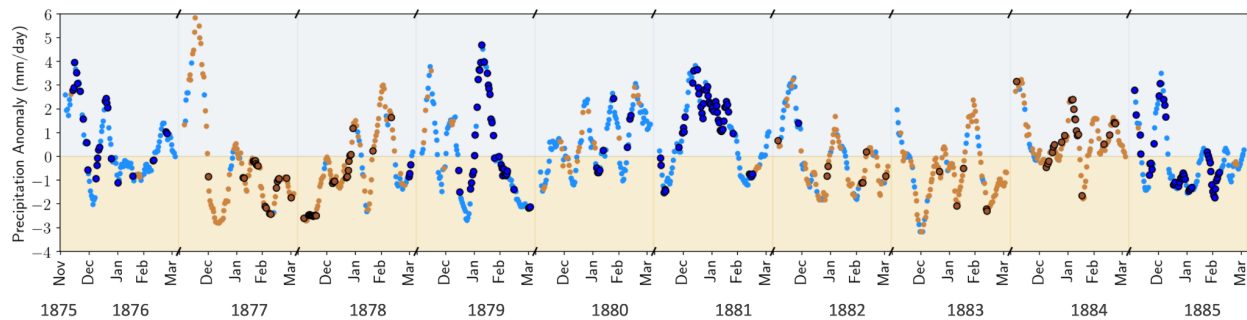


Fig 3. Time series of precipitation anomalies in Alaska from test ensemble member #9. Brown dots indicate a negative anomaly prediction. Blue dots indicate a positive anomaly prediction. Brown dots in the negative region shaded brown indicate a correctly predicted negative anomaly. Blue dots in the positive region shaded blue indicate a correctly predicted positive anomaly. Darker/larger dots outlined in black indicate the 20% most confident predictions as identified by the neural network.

### 3b. Identifying Sources of Subseasonal Predictability

Explainable AI techniques are powerful tools that allow us to not only explain the network's decision-making process, but also to identify sources of predictability. Here, we use the XAI technique, integrated gradients, described in Section 2d to locate tropical sources of subseasonal predictability for U.S. West Coast precipitation. We calculate integrated gradients heatmaps for each input map that correspond to a correct forecast-of-opportunity prediction, e.g. a prediction that was correct and in the

20% most confident range. The heatmaps are composited separately for negative and positive predictions, shown in Figure 4. Heatmaps were also clustered using k-means clustering using 2-4 clusters (not shown), but sources of predictability were similar across the clusters compared to the composited (1 cluster) heatmaps.

The XAI heatmaps shown in Figure 4 depict the regions of the input that are most relevant to the network's correct, confident predictions. Regions with the highest values (e.g. darkest shading) highlight potential sources of predictability. In both Alaska and the Pacific Northwest, the tropical western Pacific region is important for the networks' predictions, with off-equatorial bands extending east into the central Pacific. This pattern is similar to the precipitation patterns related to ENSO documented in CESM2 (Capotondi et al., 2020). Furthermore, the heatmaps reveal that the northern Maritime Continent region is relevant for negative sign predictions in Alaska and positive sign predictions in the Pacific Northwest. The Maritime Continent region is often associated with the MJO (Zhang 2005; Kang et al. 2020; Ahn et al. 2020; Kang et al. 2021), although the MJO-associated rainfall is typically more centered around the equator than the XAI heatmap highlighted region. We note that MJO convection is well represented in CESM2 (Danabasoglu et al., 2020), and do not attribute the off-equatorial region to be associated with a bias in CESM2. Since the neural networks are tasked with predicting precipitation anomalies at 21-35 day lead time, and it generally takes about 14 days for Rossby wave trains to be established from the tropics to the extratropics (Hoskins & Karoly, 1981), the expected teleconnection would be that associated with the previous one or two phases of the MJO. The Maritime Continent region is associated with active convection in MJO phases 4 and 5, which is consistent with Pacific Northwest positive precipitation anomalies in phases 2 and 3. This region is also associated with suppressed convection in phases 8 and 1, consistent with negative Pacific Northwest precipitation anomalies in phases 6 and 7, with variations based on early or late winter season (Bond & Vecchi, 2003).

For predictions over California, a major tropical source of predictability is located predominantly in the central equatorial Pacific and is most relevant for the positive sign predictions, whereas the central Indian Ocean is found to be a more prominent source of predictability for negative sign predictions. This region is associated with active convection during MJO phase 2 and 3 which is consistent with negative rainfall anomalies in California particularly during El Niño events (Arcodia et al., 2020).

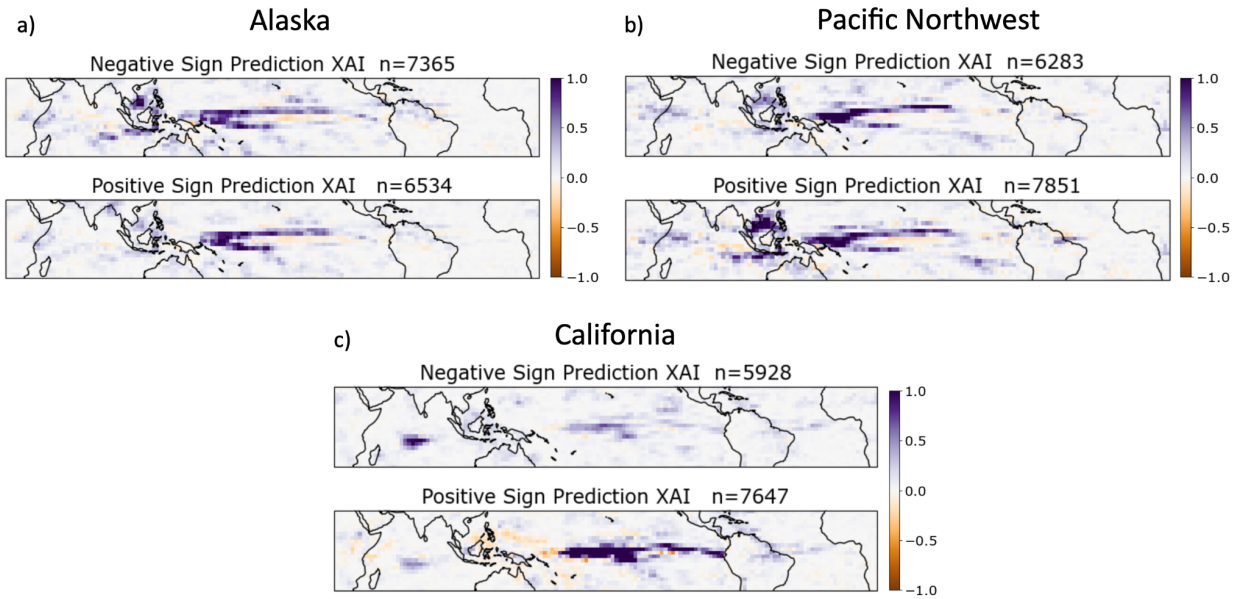


Fig 4. Integrated gradients XAI composited heatmaps for a) Alaska, b) Pacific Northwest, and c) California for the 20% most confident and correct negative (top) and positive (bottom) predictions. The number (n) represents the number of samples in each composite. Darker purple colors represent grid cells that were more relevant to the prediction, orange/brown colors represent adverse contributions to the predictions. Colorbars indicate a unitless measure of relevance.

### 3c. Decadal Variability of Subseasonal Predictability

The XAI analysis has identified physically relevant tropical sources of predictability that allow us to build trust in the neural networks predictions and its ability to identify forecasts of opportunity. These predictions are next assessed to determine if the subseasonal predictability quantified by the networks varies on decadal timescales, with periods of higher and lower skill than the overall averaged accuracy. The accuracy of the networks' predictions is calculated over a 10-year moving window (Fig. 5), as opposed to the full 100-year period for which the accuracy was calculated in Figure 1. For example, the accuracy of all test members for each experiment is first calculated over a 10-year period (1851-1860), then shifted forward 1 year (1852-1861), etc. to create the low-frequency time series of the accuracy in each region (gray lines). The time series is centered around the 10-year period for which the accuracy is calculated (e.g. the point corresponding to 1860 was calculated over 1856-1865). Figure 5 shows the accuracy time series for one test ensemble member for each region, with each individual line representing

one random seed and the dark line representing the average over the random seeds. Supplemental Figure S2-4 shows the time series for each of the ten testing ensemble members. The same moving averaging process is repeated for the 20% most confident predictions (purple lines) and the 20% least confident predictions (blue lines). That is, the 20% most confident and least confident samples are selected from each 10-year window, and then the accuracy of those samples is computed.

The variability of the 20% least confident predictions (blue lines) in Figure 5, show little decadal variability with accuracies remaining consistent around 50% (e.g. random chance). Decadal variability of the 20% most confident predictions (purple lines) is much more pronounced than the accuracy of all predictions (gray lines), suggesting the decadal variability in accuracy from all predictions is mainly from the decadal variability of the accuracy of confident predictions. For all three regions, the 10-year averaged accuracy ranges between approximately 40%-80%. Based on the sources of predictability identified in Figure 4, the forecasts of opportunity occur when certain conditions are present in the highlighted regions, but the accuracy of these forecasts of opportunity varies on decadal timescales. For example, during the late 1890s in Alaska, the 10-year average accuracy was over 70%, but the accuracy dropped to almost 40% (worse than random chance) during the late 1880s. Similar low frequency variability in accuracy is found in the Pacific Northwest and California during forecasts of opportunity. This variability implies that there is a low frequency modulation of subseasonal prediction skill for midlatitude precipitation driven by the tropics.

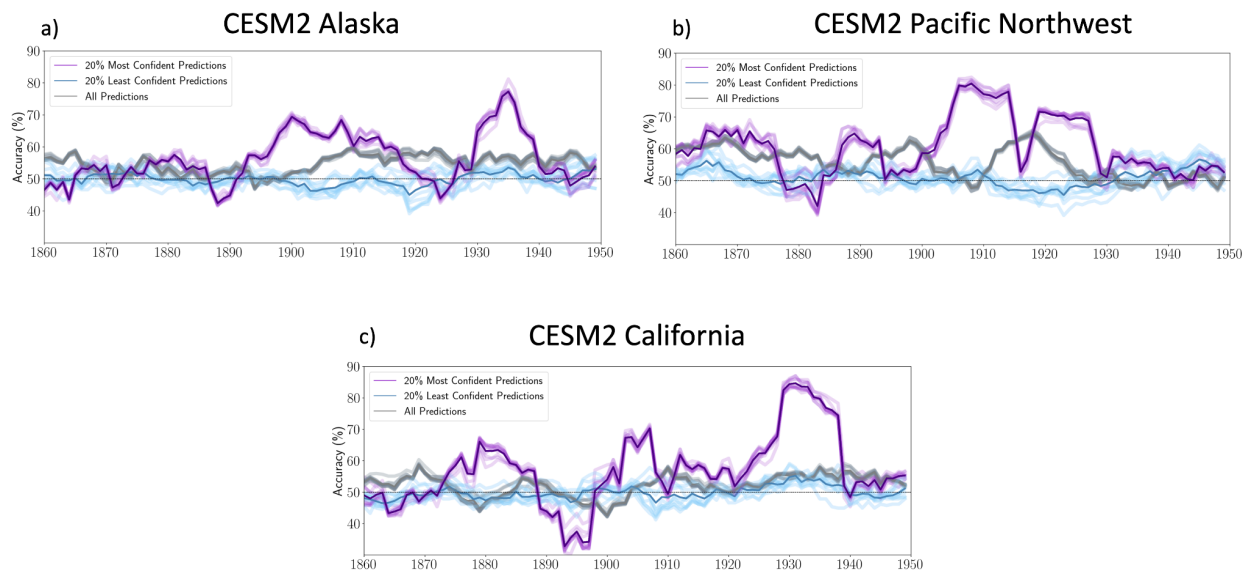


Fig 5. 10-year moving windows of accuracy shifted forward by 1 year for 10 random seeds of one CESM2 test ensemble member for all predictions (gray), the 20% most confident predictions (purple), and the 20% least confident predictions (blue) for a) Alaska, b) Pacific Northwest, and c) California. Darker lines represent the average of the 10 random seeds.

We investigate the drivers of the low frequency variability of the subseasonal prediction skill, focusing explicitly on forecasts of opportunity. Although the 20% most confident predictions have the highest accuracy overall (Fig. 2), these predictions also exhibit the largest variability with periods of both the highest and lowest skill (Fig. 5). The daily tropical precipitation input maps corresponding to the 20% most confident predictions were composited by sign of the true anomaly in the predicted region and by maps which resulted in correct and incorrect predictions, resulting in four composite maps for each region (Fig. 6). In California, correct predictions for a negative anomaly correspond to negative precipitation anomalies in the tropical Pacific, typically associated with a La Niña precipitation pattern (Dai & Wigley, 2000). Correct predictions for a positive anomaly correspond to the opposite pattern with positive tropical precipitation anomalies, typically associated with an El Niño precipitation pattern (Dai & Wigley, 2000). However, when the network is confident and *incorrect*, the network uses the learned relationship between the tropics and the sign of mid latitude precipitation, but the true sign is now opposite. In other words, when a La Niña-type pattern is present in the equatorial Pacific, the network will confidently predict a negative anomaly, but the true anomaly will be positive, and vice versa for an El Niño-type pattern. A similar relationship is found for Alaska while an opposite-signed relationship is found in the Pacific Northwest: an El Niño-like pattern corresponds to a negative sign prediction and a La Niña-like pattern corresponds to a positive sign prediction. This contrasting relationship with ENSO between California and the Pacific Northwest precipitation anomalies is consistent with previous literature on ENSO teleconnections (Diaz et al., 2001; Evans et al., 1998). These results suggest that the network has confidently learned a relationship between tropical and extratropical precipitation that is only present during specific low frequency time periods.

We find the neural networks are highly confident and accurate in its predictions during periods when the tropical-extratropical teleconnection is present from the tropical sources of predictability to the predictand midlatitude region. However, when there is a learned signal in the tropical source of predictability but that teleconnection is not present, the network will still be confident, but inaccurate in its predictions (Fig. 6). Based on these results, we can conclude that the teleconnection from the tropics to the extratropics is modulated on low frequency timescales, driving the periods of high and low subseasonal prediction skill.

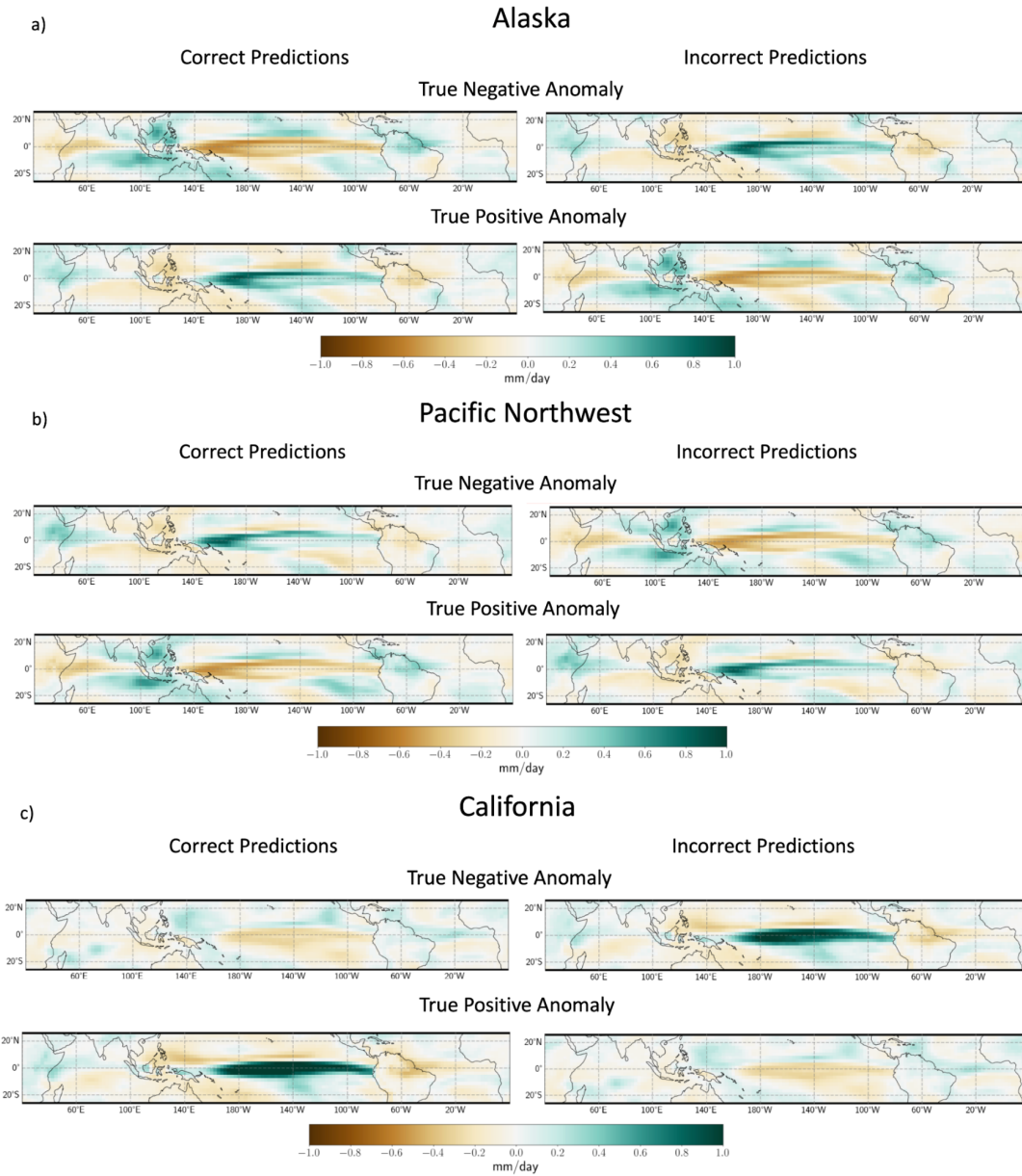


Fig. 6. Composite maps of the input precipitation anomalies (mm day<sup>-1</sup>) for days that corresponded to the 20% most confident and correct predictions (left) and incorrect predictions (right) for a true negative anomaly (top) and a true positive anomaly (bottom) for a) Alaska, b) Pacific Northwest, and c) California using the CESM-2 data.

### 3d. Predictability within ERA5

The neural networks described thus far were trained, validated, and tested on the CESM2-LE for the time period between 1850-1949. The network's task was straightforward in that it was trained on 100 years of



data and tested on data from the same climate model. Since climate models are known to have biases and deficiencies (Danabasoglu et al., 2020), we explore whether the relationships learned by the network in the CESM2-LE historical simulation apply to the ERA5 reanalysis data. That is, we do not retrain the network on the ERA5 data, but rather, we use the CESM2-trained network to make predictions on the ERA5 anomalies. We make predictions on daily ERA5 data over the years 1959-2021, and the averaged accuracies across all 100 trained networks are shown in Figure 7a.

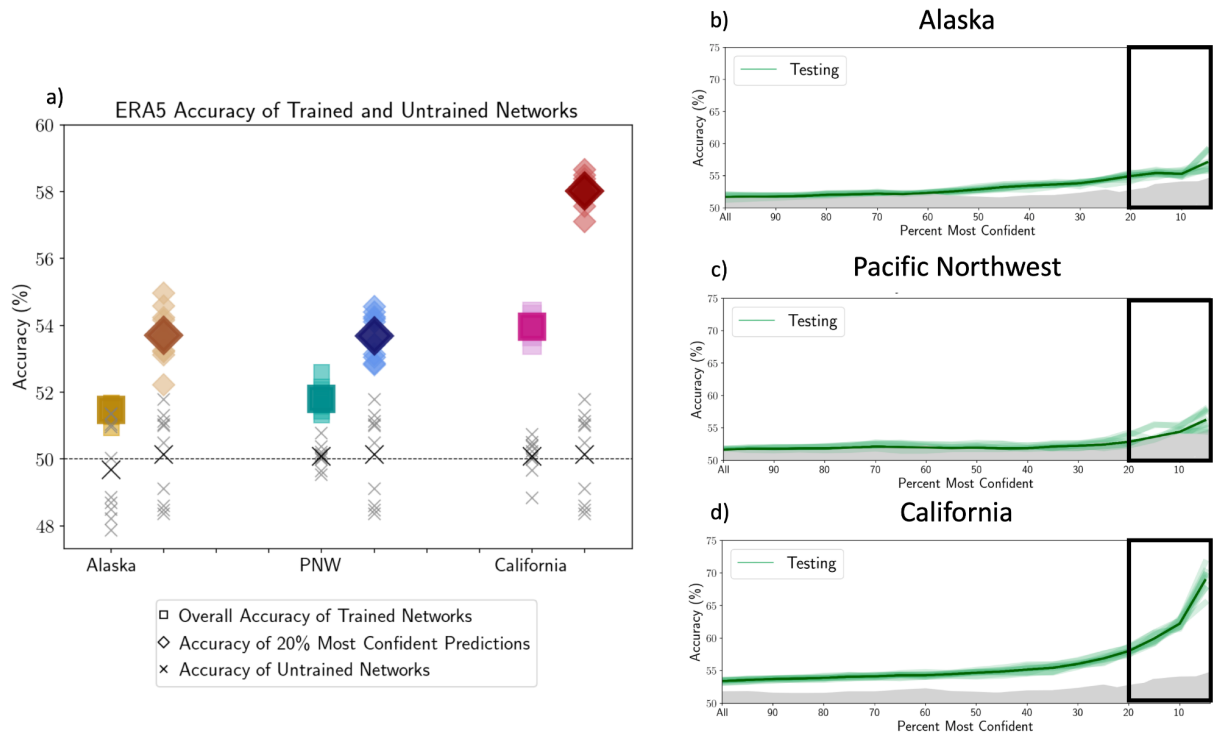


Fig. 7. a) The average accuracy of ERA5 testing data predictions for 1959-2021 for neural networks trained on CESM2 data from 1850-1949. Squares represent the average accuracy for 10 random seeds from one experiment. Large, dark squares represent the average accuracy across all 100 networks. Gray “X”s represent the average accuracy of an untrained/random network with the dark X showing the average accuracy from the random network. Note the different y-axis from that in Figure 2a. b-d) The accuracy vs. confidence for b) Alaska, c) Pacific Northwest, and d) California for 10 random seeds of one experiment for the testing data (light green lines) and the average accuracy of the testing data (dark green line) with the gray box showing the region of predictions with the 20% most confidence for each region.

We analyze the ERA5 testing data in the same way as the CESM2 data, and find the accuracies are higher

than random chance in each of the three locations. As expected, the accuracy over all of the ERA5 predictions is lower than the accuracies of the CESM2 data since the network was trained on the CESM2 data alone. Interestingly, California has notably the highest skill amongst the three predictand regions (Fig. 7). The ERA5 data used for California shows nearly the same skill as the CESM2 data, particularly for the most confident forecasts (Figs. 2a, 7a red diamonds). Figure 7 is compelling in that the networks exhibit skill above random chance, particularly for the forecasts of opportunity (diamonds). That is, the networks have identified predictable states of the climate system within CESM2, that are useful for making accurate subseasonal precipitation predictions in the real world.

We extend this analysis to assess if the ERA5 data exhibits similar decadal variability of the prediction skill as was found in the CESM2-LE historical simulation. Figure 8 shows the average accuracy from ERA5 data for each of the 10 random seeds per experiment, since the same ERA5 dataset is used for testing in each of the 10 sets of neural networks. The dark lines show the average of the 10 experiments. As with CESM2, there is also decadal variability, in the subseasonal prediction skill of ERA5 data, specifically for forecasts of opportunity, albeit with lower magnitude in the range of accuracy than in the CESM2 data. Also of note is California's high subseasonal prediction skill during the late 1970s and early 1980s, and again in the mid-to-late 1990s. The Week 4-5 precipitation anomaly prediction skill in California provided *only from the tropics* is, on average, over 65% for over a decade. The skill then drops to roughly random chance in the 2000s. In Alaska, the 1970s and early 2000s exhibit low frequency periods of high accuracy for the 20% most confident predictions compared to all predictions, with skill below random chance during the 1980s and 1990s. In the Pacific Northwest, the highest accuracy for the most confident predictions is also during the 1970s, with skill equal to below random chance in the 2000s. Consistent with the results found using the CESM2-LE historical simulations, these results show the largest decadal variability in subseasonal prediction skill occur during forecasts of opportunity.

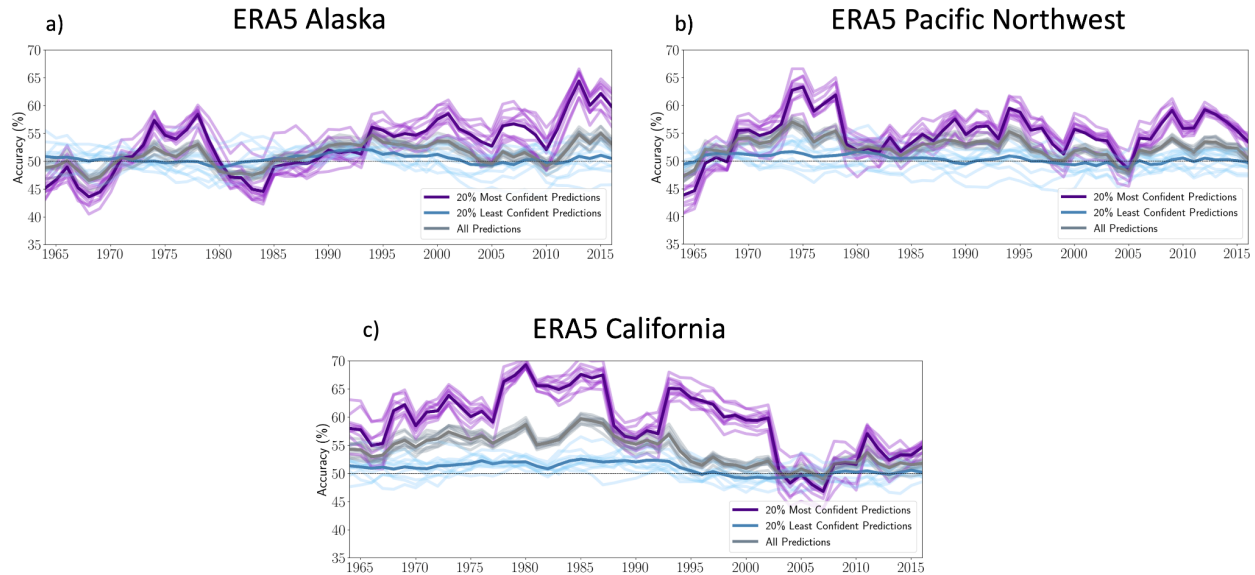


Fig. 8. 10-year moving windows of accuracy shifted forward 1 year for the ERA5 testing data for the average of 10 random seeds for all predictions (gray), the 20% most confident predictions (purple), and the 20% least confident predictions (blue) for a) Alaska, b) Pacific Northwest, and c) California. Darker lines represent the average accuracy of the 10 neural networks. Note the different y-axis from that in Figure 2.

## 4. Discussion

The decadal variability of subseasonal predictability found here is related to a low frequency modulation of the teleconnection from the tropics to the extratropics. An in-depth analysis has been conducted exploring various climate modes as drivers of the low frequency variability. The indices for extratropical variability modes (e.g., Pacific Decadal Oscillation (PDO), North Atlantic Oscillation (NAO), Pacific North America pattern (PNA), and Atlantic Multi-decadal Oscillation (AMO)) are calculated using the Program for Climate Model Diagnosis and Intercomparison (PCMDI) Metrics Package (PMP; Glecker et al. (2016; 2008); Lee et al. 2023). In particular, we applied the Common Basis Function approach that projects the observed empirical orthogonal functions (EOF) onto model anomalies (Lee et al. (2019, 2021)). For PDO and AMO, Met Office Hadley Centre Sea Ice and Sea Surface Temperature dataset (HadISST) version 1.1 (Rayner et al., (2003)) monthly sea surface temperature (SST) was used as reference observation. For NAO and PNA, sea-level pressure from the 20th Century Reanalysis (20CR; Compo et al. (2011)) was used as reference observation. For both observations, the modes are analyzed over the period 1900-2005.

Particular effort went into investigating the role of the PDO as the PDO is known to modulate rainfall variability along the West Coast on low frequency timescales (Newman et al., 2016). The correlations between the 10-year moving window of accuracy of the 20% most confident predictions and the 10-year smoothed PDO Index are shown in Supplemental Figure S6 for Alaska, but results are similar for the Pacific Northwest and California. We find that the correlations between the PDO and the accuracy of the forecasts of opportunity for different ensemble members are inconsistent, with some correlation coefficients of the same magnitude but opposite sign between test members. Similar correlation calculations between the timeseries of the low frequency accuracy and the AMO, NAO, and PNA indices are computed and, as was found with the PDO, we find little-to-no consistent relationship between decadal variability of subseasonal predictability and the AMO, NAO or PNA. Related to our findings, Oliver (2015) showed that while the relationship between the MJO and Alaska surface air temperature varies on multidecadal timescales, the PDO is not fully responsible for the variability. Oliver (2015) did find a weak negative correlation between MJO-related midlatitude air temperature variability and the PDO in observations. This suggests the correlation found in Oliver (2015) may be related to the forced response and not internal variability analyzed using the CESM2 data, but further investigation is required. Moreover, Geert Jan van Oldenborgh (2005) found that decadal fluctuations in ENSO teleconnections, particularly for precipitation, can be explained only by random statistical fluctuations of a constant teleconnection, suggesting that the low frequency variability may be, in part, stochastically driven.

Relationships between the PDO and ENSO have also been shown to affect low-frequency variability of North American precipitation (Fuentes-Franco et al., 2016; Gershunov & Barnett, 1998; Maher Nicola Kay Jennifer & Capotondi, 2022). Additional work looking at the frequency of the PDO, ENSO, and PDO+ENSO in-phase periods with high or low accuracy was performed, but results were not significant to show that a PDO-ENSO phase relationship was fully responsible for variability in the subseasonal midlatitude prediction skill. Based on these additional climate mode analyses, it is likely that low frequency modulation of the tropical-extratropical teleconnection is not solely related to one particular climate mode of variability.

Decadal modulation of the MJO and ENSO has been documented (Burgman et al., 2008; Gushchina & Dewitte, 2019), and teleconnectivity between the tropics and the midlatitudes has been shown to vary based on both MJO and ENSO phase (Kim, 2020; Tseng et al., 2020). Furthermore, decadal variability of MJO teleconnections in boreal winter has been shown to be associated with changes in both the MJO tropical heating and the mean state via the jetstream as a waveguide (Kim, 2020). Ambrizzi et al. (1995) also found that regions of teleconnectivity tend to be co-located with the jets. Investigation of the role of

the jet as the main determinant of the teleconnectivity between tropical and extratropical precipitation on decadal timescales is left for future work. Further investigation into the drivers responsible for the low frequency teleconnection modulation could help enhance high prediction skill in the midlatitudes provided by the tropics.

## 5. Conclusions

Artificial neural networks are employed to quantify subseasonal midlatitude prediction skill of U.S. West Coast precipitation provided by the tropics and assess variability of this skill on decadal timescales. We find that as the confidence of the networks increases, the accuracy increases, indicating that the networks can identify more predictable states of the climate system that result in forecasts with higher skill. Thus, we leverage the network's confidence in its predictions to identify subseasonal forecasts of opportunity, defined here as the 20% most confident predictions. An explainable artificial intelligence (XAI) method, integrated gradients, identifies regions in the tropical input maps which were most relevant to a neural network making a confident and correct prediction. These highlighted locations are found in regions associated with the MJO and ENSO, consistent with previous literature noting these climate modes can produce subseasonal forecasts of opportunity when active (Arcodia et al., 2020; DeFlorio et al., 2019; Johnson et al., 2014; Tseng et al., 2020). These results suggest the network is identifying physically meaningful sources of midlatitude subseasonal predictability.

Using these networks, we find that subseasonal prediction skill provided by the tropics can vary on decadal timescales within the CESM2-LE historical simulations. The network-identified forecasts of opportunity exhibit the highest variability of accuracy, with periods of considerably higher and lower accuracy than the average of all predictions from the same time period. Thus, there are low frequency time periods in which the tropics provide large prediction skill to subseasonal midlatitude precipitation prediction. Moreover, there is a limit to the amount of prediction skill provided by the tropics on decadal timescales in this neural network framework as demonstrated by periods with forecast skill that can be worse than random chance.

The neural networks trained on CESM2 data from 1850-1949 were used to test ERA5 reanalysis data from 1959-2021 to examine if the relationships learned in CESM2 are found in reanalysis. The network is skillful on ERA5 data for all three regions, particularly during forecasts of opportunity, despite the neural network being trained on a different dataset and time period. This suggests CESM2 can identify real, physical relationships between tropical and extratropical precipitation useful for subseasonal

predictability. Furthermore, the accuracy of the network for forecasts of opportunity also varies on decadal timescales in the ERA5 data, as was found in the CESM2 data. California exhibits the highest accuracy for the forecasts of opportunity in the ERA5 data, indicating that the relationships learned by the CESM-trained neural networks were most useful for California. While the last few decades have seen improvements in subseasonal prediction skill due to model advancements (Mariotti et al., 2020), we find additional regional increases in subseasonal predictability provided by the tropics during forecasts of opportunity due to decadal variability.

Notably, there is a drop in skill since the late 2000s in California, which previously had two periods of high accuracy during the mid-1970s to mid-1980s and then the mid-1990s to early-2000s. These results have implications for subseasonal midlatitude prediction skill, as we have highlighted low frequency periods in which subseasonal prediction skill provided *only from the tropics* has high accuracy (>65% in ERA5) for the most confident forecasts. Conversely, there are low frequency time periods when the most confident predictions have prediction skill worse than random chance. This variability is driven by a decadal modulation in the teleconnectivity between the tropics and the extratropics— high accuracy time periods occur when the learned teleconnection from the tropics to the midlatitude region being predicted is present, and low accuracy periods occur when the teleconnection is not present. Investigating prediction skill of the teleconnectivity between the tropics and the extratropics on decadal timescales has the potential to enhance subseasonal forecast skill, particularly for forecasts of opportunity.

## **Acknowledgements**

This study was supported by the Regional and Global Model Analysis program area of the U.S. Department of Energy's (DOE) Office of Biological and Environmental Research (BER) as part of the Program for Climate Model Diagnosis and Intercomparison project. The work conducted by KJM is based upon research supported by the U.S. Department of Energy, Office of Science, Office of Biological & Environmental Research (BER), Regional and Global Model Analysis (RGMA) component of the Earth and Environmental System Modeling Program under Award Number DE-SC0022070. KJM was additionally funded, in part, by the National Science Foundation Graduate Research Fellowship under Grant 006784. Lastly, this work was supported by the National Center for Atmospheric Research (NCAR), which is a major facility sponsored by the NSF under Cooperative Agreement No. 1852977. The work of LLNL-affiliated authors were performed under the auspices of the U.S. Department of Energy (DOE) by Lawrence Livermore National Laboratory under contract No. DE-AC52-07NA27344

and supported by the Regional and Global Model Analysis (RGMA) program of the U.S. DOE, Office of Science, Office of Biological and Environmental Research. Support for the 20CR Project dataset is provided by the U.S. DOE, Office of Science Innovative and Novel Computational Impact on Theory and Experiment (DOE INCITE) program, and Office of Biological and Environmental Research (BER), and by the National Oceanic and Atmospheric Administration Climate Program Office. The authors would like to thank Antonios Mamalakis for helpful discussions.

## **Data Availability**

CESM2 Large Ensemble Data are available freely to the public at <https://www.cesm.ucar.edu/community-projects/lens2>. ERA5 data are available freely at <https://cds.climate.copernicus.eu/>.

All Python code for processing data and figures for this analysis is available at [www.github.com/mbarcodia/ERC23\\_paper\\_code](http://www.github.com/mbarcodia/ERC23_paper_code). At the time of publication, this will be converted to a permanent repository on Zenodo.

PMP source code is available on GitHub ([https://github.com/PCMDI/pcmdi\\_metrics](https://github.com/PCMDI/pcmdi_metrics)) with DOI number assigned by Zenodo at <https://doi.org/10.5281/zenodo.7783324>. The Twentieth Century Reanalysis (20CR) data is provided by the NOAA/Earth System Research Laboratory (ESRL)/Physical Sciences Division (PSD) from their website at <http://www.esrl.noaa.gov/psd/>. The HadISST data is available through the UK Met Office's website at <http://www.metoffice.gov.uk/hadobs/hadisst/>.

## **References**

- Albers, J. R., & Newman, M. (2019). A Priori identification of skillful extratropical subseasonal forecasts. *Geophysical Research Letters*, *46*(21), 12527–12536.
- Albers, J. R., & Newman, M. (2021). Subseasonal predictability of the North Atlantic Oscillation. *Environmental Research Letters: ERL [Web Site]*, *16*(4), 044024.
- Ambrizzi, T., Hoskins, B. J., & Hsu, H.-H. (1995). Rossby Wave Propagation and Teleconnection Patterns in the Austral Winter. *Journal of the Atmospheric Sciences*, *52*(21), 3661–3672.
- Arcodia, M. C., & Kirtman, B. P. (2022). *Using Simplified Linear and Nonlinear Models to Assess*

*ENSO-Modulated MJO Teleconnections.*

<https://www.researchsquare.com/article/rs-1766560/latest.pdf>

- Arcodia, M. C., Kirtman, B. P., & Siqueira, L. S. P. (2020). How MJO Teleconnections and ENSO Interference Impacts U.S. Precipitation. *Journal of Climate*, 33(11), 4621–4640.
- Bommer, P., Kretschmer, M., Hedström, A., Bareeva, D., & Höhne, M. M.-C. (2023). Finding the right XAI method -- A Guide for the Evaluation and Ranking of Explainable AI Methods in Climate Science. In *arXiv [cs.LG]*. arXiv. <http://arxiv.org/abs/2303.00652>
- Bond, N. A., & Vecchi, G. A. (2003). The Influence of the Madden–Julian Oscillation on Precipitation in Oregon and Washington. *Weather and Forecasting*, 18(4), 600–613.
- Burgman, R. J., Schopf, P. S., & Kirtman, B. P. (2008). Decadal Modulation of ENSO in a Hybrid Coupled Model. *Journal of Climate*, 21(21), 5482–5500.
- Capotondi, A., Deser, C., Phillips, A. S., Okumura, Y., & Larson, S. M. (2020). ENSO and pacific decadal variability in the community earth system model version 2. *Journal of Advances in Modeling Earth Systems*, 12(12). <https://doi.org/10.1029/2019ms002022>
- Cassou, C. (2008). Intraseasonal interaction between the Madden-Julian Oscillation and the North Atlantic Oscillation. *Nature*, 455(7212), 523–527.
- Compo, G. P., Whitaker, J. S., Sardeshmukh, P. D., Matsui, N., Allan, R. J., Yin, X., Gleason, B. E., Vose, R. S., Rutledge, G., Bessemoulin, P., Brönnimann, S., Brunet, M., Crouthamel, R. I., Grant, A. N., Groisman, P. Y., Jones, P. D., Kruk, M. C., Kruger, A. C., Marshall, G. J., ... Worley, S. J. (2011). The twentieth century reanalysis project. *Quarterly Journal of the Royal Meteorological Society*, 137(654), 1–28.
- Dai, A., & Wigley, T. M. L. (2000). Global patterns of ENSO-induced precipitation. *Geophysical Research Letters*, 27(9), 1283–1286.
- Danabasoglu, G., Lamarque, J.-F., Bacmeister, J., Bailey, D. A., DuVivier, A. K., Edwards, J., Emmons, L. K., Fasullo, J., Garcia, R., Gettelman, A., Hannay, C., Holland, M. M., Large, W. G., Lauritzen, P. H., Lawrence, D. M., Lenaerts, J. T. M., Lindsay, K., Lipscomb, W. H., Mills, M. J., ... Strand, W. G.



- (2020). The community earth system model version 2 (CESM2). *Journal of Advances in Modeling Earth Systems*, 12(2). <https://doi.org/10.1029/2019ms001916>
- DeFlorio, M. J., Waliser, D. E., Ralph, F. M., Guan, B., Goodman, A., Gibson, P. B., Asharaf, S., Monache, L. D., Zhang, Z., Subramanian, A. C., Vitart, F., Lin, H., & Kumar, A. (2019). Experimental subseasonal-to-seasonal (S2S) forecasting of atmospheric rivers over the western United States. *Journal of Geophysical Research*, 124(21), 11242–11265.
- Diaz, H. F., Hoerling, M. P., & Eischeid, J. K. (2001). ENSO variability, teleconnections and climate change. *International Journal of Climatology*, 21(15), 1845–1862.
- Evans, M. N., Fairbanks, R. G., & Rubenstone, J. L. (1998). A proxy index of ENSO teleconnections. *Nature*, 394(6695), 732–733.
- Fuentes-Franco, R., Giorgi, F., Coppola, E., & Kucharski, F. (2016). The role of ENSO and PDO in variability of winter precipitation over North America from twenty first century CMIP5 projections. *Climate Dynamics*, 46(9), 3259–3277.
- Geert Jan van Oldenborgh, G. B. (2005). Searching for decadal variations in ENSO precipitation teleconnections. *Geophysical Research Letters*. <https://doi.org/10.1029/2005GL023110>
- Gershunov, A., & Barnett, T. P. (1998). Interdecadal Modulation of ENSO Teleconnections. *Bulletin of the American Meteorological Society*, 79(12), 2715–2726.
- Gleckler, P., Doutriaux, C., Durack, P., Taylor, K., Zhang, Y., Williams, D., Mason, E., & Servonnat, J. (2016). A more powerful reality test for climate models. *Eos*, 97. <https://doi.org/10.1029/2016eo051663>
- Gordon, E. M., Barnes, E. A., & Hurrell, J. W. (2021). Oceanic harbingers of pacific decadal oscillation predictability in CESM2 detected by neural networks. *Geophysical Research Letters*, 48(21). <https://doi.org/10.1029/2021gl095392>
- Gushchina, D., & Dewitte, B. (2019). Decadal modulation of the relationship between intraseasonal tropical variability and ENSO. *Climate Dynamics*, 52(3), 2091–2103.
- Ham, Y.-G., Kim, J.-H., & Luo, J.-J. (2019). Deep learning for multi-year ENSO forecasts. *Nature*,

573(7775), 568–572.

Hersbach, H., Bell, B., Berrisford, P., Hirahara, S., Horányi, A., Muñoz-Sabater, J., Nicolas, J., Peubey, C., Radu, R., Schepers, D., Simmons, A., Soci, C., Abdalla, S., Abellan, X., Balsamo, G., Bechtold, P., Biavati, G., Bidlot, J., Bonavita, M., ... Jean-Noël Thépaut. (2020). The ERA5 global reanalysis. *Quarterly Journal of the Royal Meteorological Society*, 146(730), 1999–2049.

Hoskins, B. J., & Karoly, D. J. (1981). The Steady Linear Response of a Spherical Atmosphere to Thermal and Orographic Forcing. *Journal of the Atmospheric Sciences*, 38(6), 1179–1196.

Huang, H., Patricola, C. M., Bercos-Hickey, E., Zhou, Y., Rhoades, A., Risser, M. D., & Collins, W. D. (2021). Sources of subseasonal-to-seasonal predictability of atmospheric rivers and precipitation in the western United States. *Journal of Geophysical Research*, 126(6).

<https://doi.org/10.1029/2020jd034053>

Johnson, N. C., Collins, D. C., Feldstein, S. B., L'Heureux, M. L., & Riddle, E. E. (2014). Skillful Wintertime North American Temperature Forecasts out to 4 Weeks Based on the State of ENSO and the MJO. *Weather and Forecasting*, 29(1), 23–38.

Jones, C., & Carvalho, L. M. V. (2012). Spatial–Intensity Variations in Extreme Precipitation in the Contiguous United States and the Madden–Julian Oscillation. *Journal of Climate*, 25(14), 4898–4913.

Kang, D., Kim, D., Ahn, M.-S., Neale, R., Lee, J., & Gleckler, P. J. (2020). The role of the mean state on MJO simulation in CESM2 ensemble simulation. *Geophysical Research Letters*, 47(24).

<https://doi.org/10.1029/2020gl089824>

Kim, H. (2020). *Mechanisms for the Decadal Change of the MJO Teleconnection over the Northern Hemisphere in Boreal Winter* [Graduate School of UNIST].

<https://scholarworks.unist.ac.kr/handle/201301/31779>

Labe, Z. M., & Barnes, E. A. (2022). Predicting slowdowns in decadal climate warming trends with explainable neural networks. *Geophysical Research Letters*, 49(9).

<https://doi.org/10.1029/2022gl098173>

- Lau, W. K. M., Waliser, D. E., & Roundy, P. E. (2012). Tropical–extratropical interactions. In W. K.-M. Lau & D. E. Waliser (Eds.), *Intraseasonal Variability in the Atmosphere-Ocean Climate System* (pp. 497–512). Springer Berlin Heidelberg.
- Lee, J., Sperber, K. R., Gleckler, P. J., Bonfils, C. J. W., & Taylor, K. E. (2019). Quantifying the agreement between observed and simulated extratropical modes of interannual variability. *Climate Dynamics*, *52*(7), 4057–4089.
- Lee, J., Sperber, K. R., Gleckler, P. J., Taylor, K. E., & Bonfils, C. J. W. (2021). Benchmarking Performance Changes in the Simulation of Extratropical Modes of Variability across CMIP Generations. *Journal of Climate*, *34*(17), 6945–6969.
- Lee, R. W., Woolnough, S. J., Charlton-Perez, A. J., & Vitart, F. (2019). ENSO modulation of MJO teleconnections to the north Atlantic and Europe. *Geophysical Research Letters*, *46*(22), 13535–13545.
- Ling, J., Li, C., Li, T., Jia, X., Khouider, B., Maloney, E., Vitart, F., Xiao, Z., & Zhang, C. (2017). Challenges and Opportunities in MJO Studies. *Bulletin of the American Meteorological Society*, *98*(2), ES53–ES56.
- Lovejoy, S. (2018). Spectra, intermittency, and extremes of weather, macroweather and climate. *Scientific Reports*, *8*(1), 12697.
- Luo, B., Luo, D., Dai, A., Simmonds, I., & Wu, L. (2022). Decadal variability of winter warm arctic-cold Eurasia dipole patterns modulated by pacific decadal oscillation and Atlantic multidecadal oscillation. *Earth's Future*, *10*(1). <https://doi.org/10.1029/2021ef002351>
- Madden, R. A., & Julian, P. R. (1971). Detection of a 40–50 Day Oscillation in the Zonal Wind in the Tropical Pacific. *Journal of the Atmospheric Sciences*, *28*(5), 702–708.
- Maher Nicola Kay Jennifer, & Capotondi, A. (2022). Modulation of ENSO teleconnections over North America by the Pacific decadal oscillation. *Environmental Research Letters: ERL [Web Site]*, *17*(11). <https://doi.org/10.1088/1748-9326/ac9327>
- Mamalakis, A., Barnes, E. A., & Ebert-Uphoff, I. (2022). Investigating the Fidelity of Explainable

- Artificial Intelligence Methods for Applications of Convolutional Neural Networks in Geoscience. *Artificial Intelligence for the Earth Systems*, 1(4). <https://doi.org/10.1175/AIES-D-22-0012.1>
- Mamalakis, A., Barnes, E. A., & Ebert-Uphoff, I. (2023). Carefully Choose the Baseline: Lessons Learned from Applying XAI Attribution Methods for Regression Tasks in Geoscience. *Artificial Intelligence for the Earth Systems*, 2(1). <https://doi.org/10.1175/AIES-D-22-0058.1>
- Mamalakis, A., Ebert-Uphoff, I., & Barnes, E. A. (2021). Neural Network Attribution Methods for Problems in Geoscience: A Novel Synthetic Benchmark Dataset. In *arXiv [physics.geo-ph]*. arXiv. <https://doi.org/10.1017/eds.2022>
- Mariotti, A., Baggett, C., Barnes, E. A., Becker, E., Butler, A., Collins, D. C., Dirmeyer, P. A., Ferranti, L., Johnson, N. C., Jones, J., Kirtman, B. P., Lang, A. L., Molod, A., Newman, M., Robertson, A. W., Schubert, S., Waliser, D. E., & Albers, J. (2020). Windows of Opportunity for Skillful Forecasts Subseasonal to Seasonal and Beyond. *Bulletin of the American Meteorological Society*, 101(5), E608–E625.
- Mariotti, A., Barnes, E. A., K.-M. Chang, E., Lang, A., Dirmeyer, P. A., Pegion, K., Barrie, D., & Baggett, C. (2019, February 19). Bridging the weather-to-climate prediction gap. *EOS*, 100.
- Martin, Z. K., Barnes, E. A., & Maloney, E. (2022). Using simple, explainable neural networks to predict the madden-Julian oscillation. *Journal of Advances in Modeling Earth Systems*, 14(5). <https://doi.org/10.1029/2021ms002774>
- Matthews, A. J., Hoskins, B. J., & Masutani, M. (2004). The global response to tropical heating in the Madden–Julian oscillation during the northern winter. *Quarterly Journal of the Royal Meteorological Society*, 130(601), 1991–2011.
- Mayer, K. J., & Barnes, E. A. (2021). Subseasonal forecasts of opportunity identified by an explainable neural network. *Geophysical Research Letters*, 48(10). <https://doi.org/10.1029/2020gl092092>
- Mayer, K. J., & Barnes, E. A. (2022). Quantifying the effect of climate change on midlatitude subseasonal prediction skill provided by the tropics. *Geophysical Research Letters*, 49(14). <https://doi.org/10.1029/2022gl098663>

- McGovern, A., Lagerquist, R., Gagne, D. J., Eli Jergensen, G., Elmore, K. L., Homeyer, C. R., & Smith, T. (2019). Making the Black Box More Transparent: Understanding the Physical Implications of Machine Learning. *Bulletin of the American Meteorological Society*, *100*(11), 2175–2199.
- Meehl, G. A., Richter, J. H., Teng, H., Capotondi, A., Cobb, K., Doblas-Reyes, F., Donat, M. G., England, M. H., Fyfe, J. C., Han, W., Kim, H., Kirtman, B. P., Kushnir, Y., Lovenduski, N. S., Mann, M. E., Merryfield, W. J., Nieves, V., Pegion, K., Rosenbloom, N., ... Xie, S.-P. (2021). Initialized Earth System prediction from subseasonal to decadal timescales. *Nature Reviews Earth & Environment*, *2*(5), 340–357.
- Moon, J.-Y., Wang, B., & Ha, K.-J. (2011). ENSO regulation of MJO teleconnection. *Climate Dynamics*, *37*(5), 1133–1149.
- N. A. Rayner, D. E. Parker, E. B. Horton, C. K. Folland, L. V. Alexander, D. P. Rowell, E. C. Kent, A. Kaplan. (2003). Global analyses of sea surface temperature, sea ice, and night marine air temperature since the late nineteenth century. *Journal of Geophysical Research Atmospheres*.  
<https://doi.org/10.1029/2002JD002670>
- National Academies of Sciences, Engineering, and Medicine, Division on Earth and Life Studies, Ocean Studies Board, Board on Atmospheric Sciences and Climate, & Committee on Developing a U.S. Research Agenda to Advance Subseasonal to Seasonal Forecasting. (2016). *Next Generation Earth System Prediction: Strategies for Subseasonal to Seasonal Forecasts*. National Academies Press.
- Newman, M., Alexander, M. A., Ault, T. R., Cobb, K. M., Deser, C., Di Lorenzo, E., Mantua, N. J., Miller, A. J., Minobe, S., Nakamura, H., Schneider, N., Vimont, D. J., Phillips, A. S., Scott, J. D., & Smith, C. A. (2016). The Pacific Decadal Oscillation, Revisited. *Journal of Climate*, *29*(12), 4399–4427.
- Newman, M., Sardeshmukh, P. D., Winkler, C. R., & Whitaker, J. S. (2003). A Study of Subseasonal Predictability. *Monthly Weather Review*, *131*(8), 1715–1732.
- Oliver, E. C. J. (2015). Multidecadal variations in the modulation of Alaska wintertime air temperature by the Madden–Julian Oscillation. *Theoretical and Applied Climatology*, *121*(1), 1–11.

- O'Malley, T., Bursztein, E., Long, J., Chollet, F., Jin, H., Invernizzi, L., & Others. (2019). *KerasTuner*.  
<https://github.com/keras-team/keras-tuner>
- O'Reilly, C. H., Heatley, J., MacLeod, D., Weisheimer, A., Palmer, T. N., Schaller, N., & Woollings, T. (2017). Variability in seasonal forecast skill of Northern Hemisphere winters over the twentieth century. *Geophysical Research Letters*, *44*(11), 5729–5738.
- Pegion, K., Becker, E. J., & Kirtman, B. P. (2022). Understanding Predictability of Daily Southeast U.S. Precipitation Using Explainable Machine Learning. *Artificial Intelligence for the Earth Systems*, *1*(4). <https://doi.org/10.1175/AIES-D-22-0011.1>
- Pegion, K., & Kirtman, B. P. (2008). The Impact of Air–Sea Interactions on the Predictability of the Tropical Intraseasonal Oscillation. *Journal of Climate*, *21*(22), 5870–5886.
- Pegion, K., Kirtman, B. P., Becker, E., Collins, D. C., LaJoie, E., Burgman, R., Bell, R., DelSole, T., Min, D., Zhu, Y., Li, W., Sinsky, E., Guan, H., Gottschalck, J., Joseph Metzger, E., Barton, N. P., Achuthavarier, D., Marshak, J., Koster, R. D., ... Kim, H. (2019). The Subseasonal Experiment (SubX): A Multimodel Subseasonal Prediction Experiment. *Bulletin of the American Meteorological Society*, *100*(10), 2043–2060.
- P. J. Gleckler, K. E. Taylor, C. Doutriaux. (2008). Performance metrics for climate models. *Journal of Geophysical Research Atmospheres*. <https://doi.org/10.1029/2007JD008972>
- Rosa, J. P. S., Guerra, D. J. D., Horta, N. C. G., Martins, R. M. F., & Lourenço, N. C. C. (2020). Overview of Artificial Neural Networks. In J. P. S. Rosa, D. J. D. Guerra, N. C. G. Horta, R. M. F. Martins, & N. C. C. Lourenço (Eds.), *Using Artificial Neural Networks for Analog Integrated Circuit Design Automation* (pp. 21–44). Springer International Publishing.
- Scaife, A. A., Arribas, A., Blockley, E., Brookshaw, A., Clark, R. T., Dunstone, N., Eade, R., Fereday, D., Folland, C. K., Gordon, M., Hermanson, L., Knight, J. R., Lea, D. J., MacLachlan, C., Maidens, A., Martin, M., Peterson, A. K., Smith, D., Vellinga, M., ... Williams, A. (2014). Skillful long-range prediction of European and North American winters. *Geophysical Research Letters*, *41*(7), 2514–2519.

- Sonneveld, M., Lguensat, R., Jones, D. C., Dueben, P. D., Brajard, J., & Balaji, V. (2021). Bridging observations, theory and numerical simulation of the ocean using machine learning. *Environmental Research Letters: ERL [Web Site]*, 16(7), 073008.
- Soulard, N., Lin, H., Derome, J., & Yu, B. (2021). Tropical forcing of the circumglobal teleconnection pattern in boreal winter. *Climate Dynamics*, 57(3), 865–877.
- Stan, C., Straus, D. M., Frederiksen, J. S., Lin, H., Maloney, E. D., & Schumacher, C. (2017). Review of tropical-extratropical teleconnections on intraseasonal time scales. *Reviews of Geophysics*, 55(4), 902–937.
- Sundararajan, M., Taly, A., & Yan, Q. (2017). *Axiomatic Attribution for Deep Networks*. 70, 3319–3328.
- Toms, B. A., Barnes, E. A., & Ebert-Uphoff, I. (2020). Physically interpretable neural networks for the geosciences: Applications to earth system variability. *Journal of Advances in Modeling Earth Systems*, 12(9). <https://doi.org/10.1029/2019ms002002>
- Tseng, K.-C., Maloney, E., & Barnes, E. A. (2020). The consistency of MJO teleconnection patterns on interannual time scales. *Journal of Climate*, 33(9), 3471–3486.
- van Straaten, C., Whan, K., Coumou, D., van den Hurk, B., & Schmeits, M. (2023). Correcting sub-seasonal forecast errors with an explainable ANN to understand misrepresented sources of predictability of European summer temperatures. *Artificial Intelligence for the Earth Systems*, -1(aop), 1–49.
- Vitart, F. (2017). Madden—Julian Oscillation prediction and teleconnections in the S2S database. *Quarterly Journal of the Royal Meteorological Society*, 143(706), 2210–2220.
- Vitart, F., Ardilouze, C., Bonet, A., Brookshaw, A., Chen, M., Codorean, C., Déqué, M., Ferranti, L., Fucile, E., Fuentes, M., Hendon, H., Hodgson, J., Kang, H.-S., Kumar, A., Lin, H., Liu, G., Liu, X., Malguzzi, P., Mallas, I., ... Zhang, L. (2017). The Subseasonal to Seasonal (S2S) Prediction Project Database. *Bulletin of the American Meteorological Society*, 98(1), 163–173.
- Weickmann, K. M. (1983). Intraseasonal Circulation and Outgoing Longwave Radiation Modes During Northern Hemisphere Winter. *Monthly Weather Review*, 111(9), 1838–1858.

Weisheimer, A., Schaller, N., O'Reilly, C., MacLeod, D. A., & Palmer, T. (2017). Atmospheric seasonal forecasts of the twentieth century: multi-decadal variability in predictive skill of the winter North Atlantic Oscillation (NAO) and their potential value for extreme event attribution. *Quarterly Journal of the Royal Meteorological Society*, 143(703), 917–926.

Zhang, C. (2005). Madden-Julian oscillation. *Reviews of Geophysics*, 43(2).

<https://doi.org/10.1029/2004rg000158>

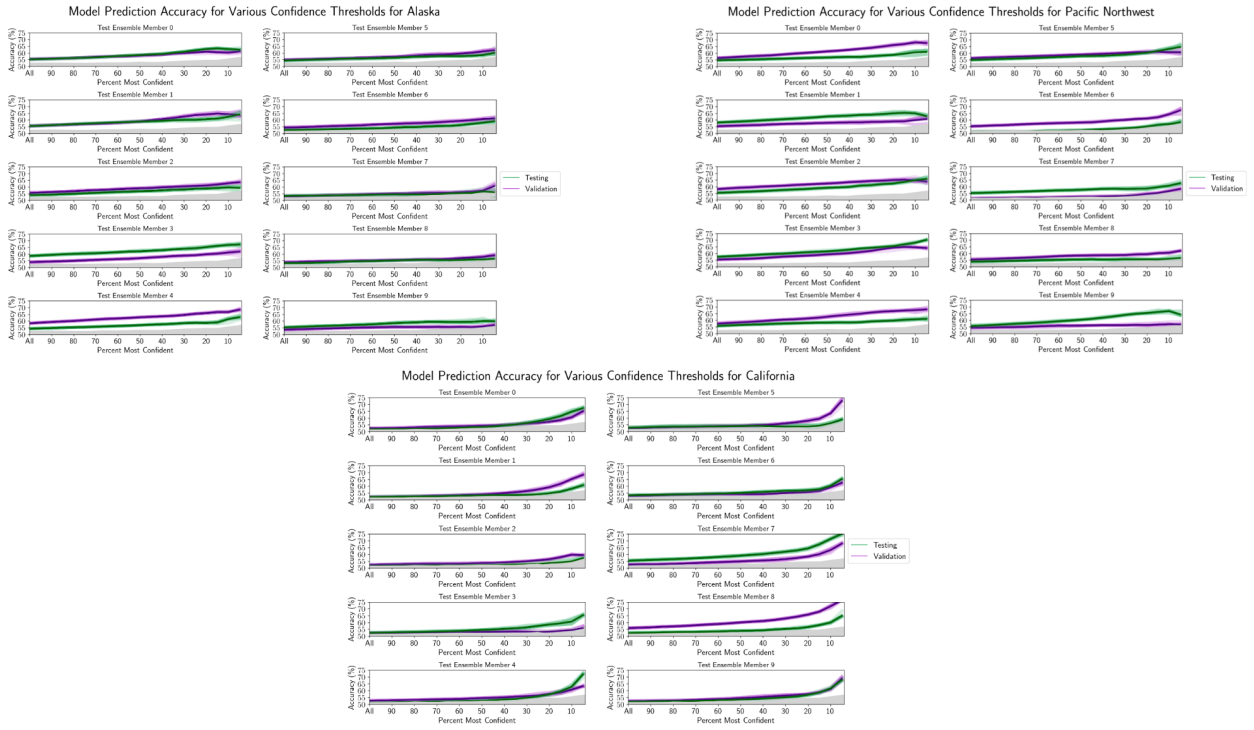
Zhang, C. (2013). Madden–Julian Oscillation: Bridging Weather and Climate. *Bulletin of the American Meteorological Society*, 94(12), 1849–1870.

## Supplemental Material

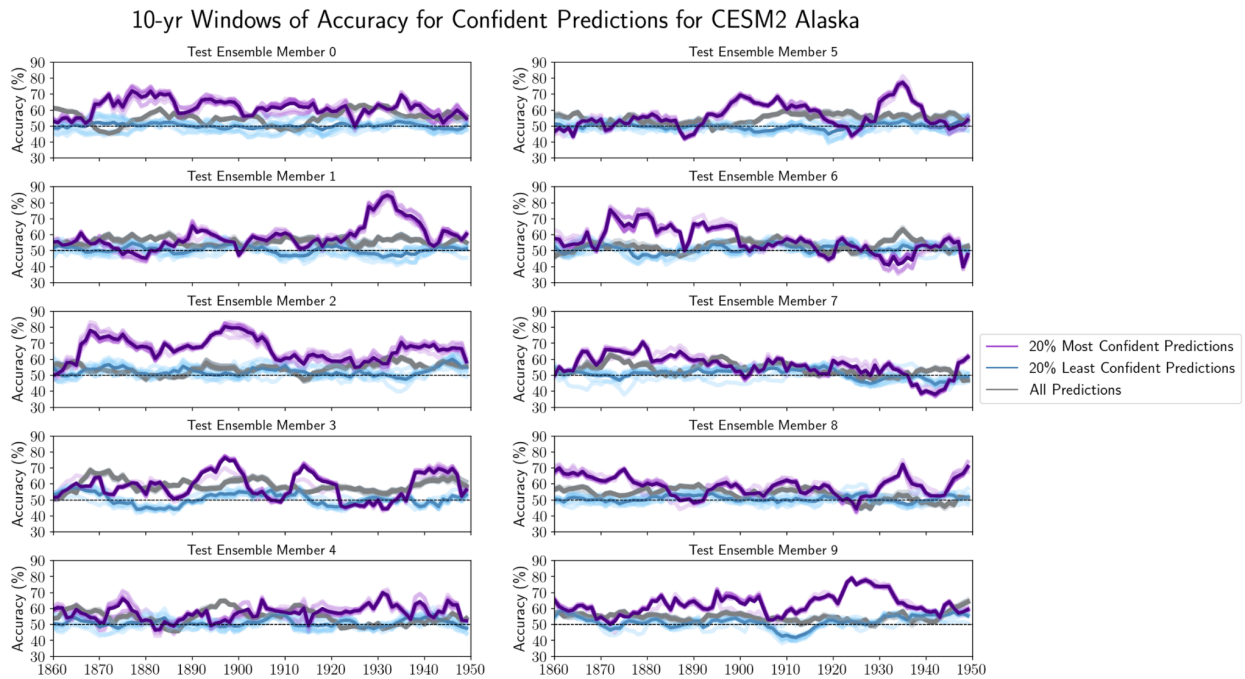
Ensemble Member Number	CESM2 Ensemble Member Name
0	b.e21.BHISTsmbb.f09_g17.LE2-1231.011.cam.h1.PRECT.1850-1949.nc
1	b.e21.BHISTsmbb.f09_g17.LE2-1231.012.cam.h1.PRECT.1850-1949.nc
2	b.e21.BHISTsmbb.f09_g17.LE2-1251.013.cam.h1.PRECT.1850-1949.nc
3	b.e21.BHISTsmbb.f09_g17.LE2-1251.014.cam.h1.PRECT.1850-1949.nc
4	b.e21.BHISTsmbb.f09_g17.LE2-1281.015.cam.h1.PRECT.1850-1949.nc
5	b.e21.BHISTsmbb.f09_g17.LE2-1281.016.cam.h1.PRECT.1850-1949.nc
6	b.e21.BHISTsmbb.f09_g17.LE2-1301.017.cam.h1.PRECT.1850-1949.nc
7	b.e21.BHISTsmbb.f09_g17.LE2-1301.018.cam.h1.PRECT.1850-1949.nc
8	b.e21.BHISTsmbb.f09_g17.LE2-1281.017.cam.h1.PRECT.1850-1949.nc
9	b.e21.BHISTsmbb.f09_g17.LE2-1251.019.cam.h1.PRECT.1850-1949.nc

Supplementary Table 1. The naming convention used in the study and the corresponding CESM2 ensemble member. Note that 1850-1949 is in italics because data are only available in 10-year increments, so the data was downloaded then concatenated for the full 1850-1949 timeseries.

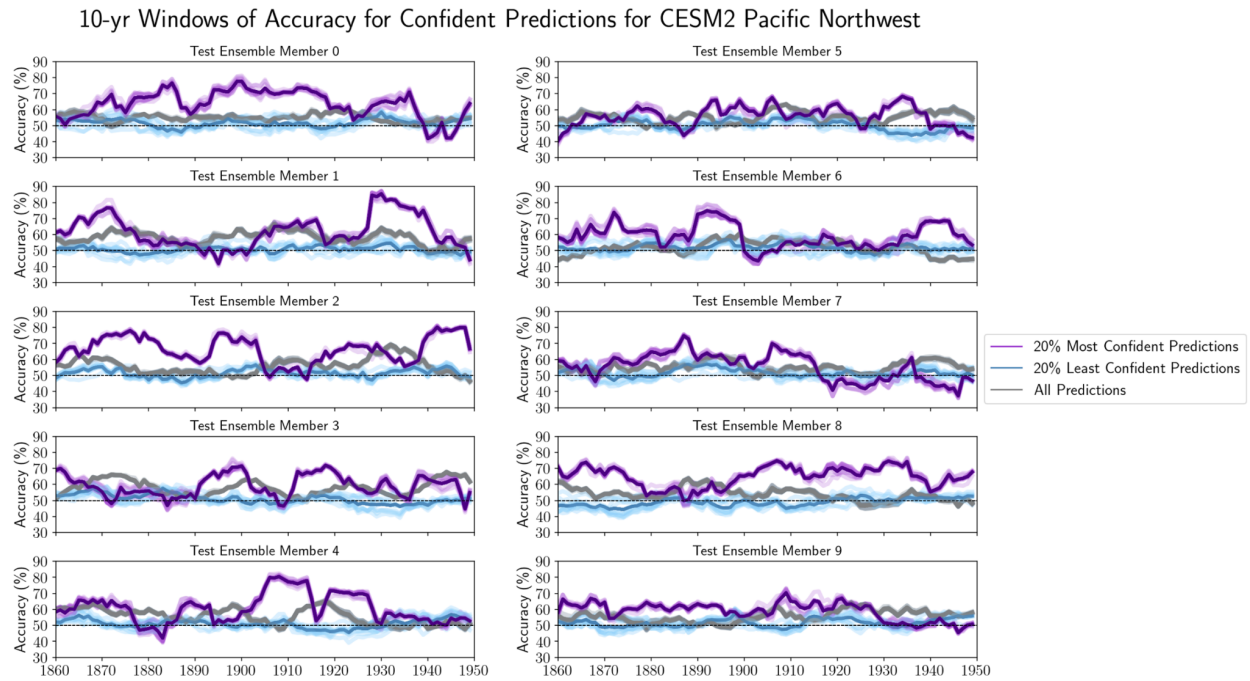




Supplemental Figure S1. Accuracy versus confidence for all ten experiments using CESM2 data for a) Alaska, b) Pacific Northwest, and c) California. Purple lines show the accuracy for the validation data for ten random seeds for each experiment and dark purple lines show the average of the random seeds. Green lines show the same but for testing data.

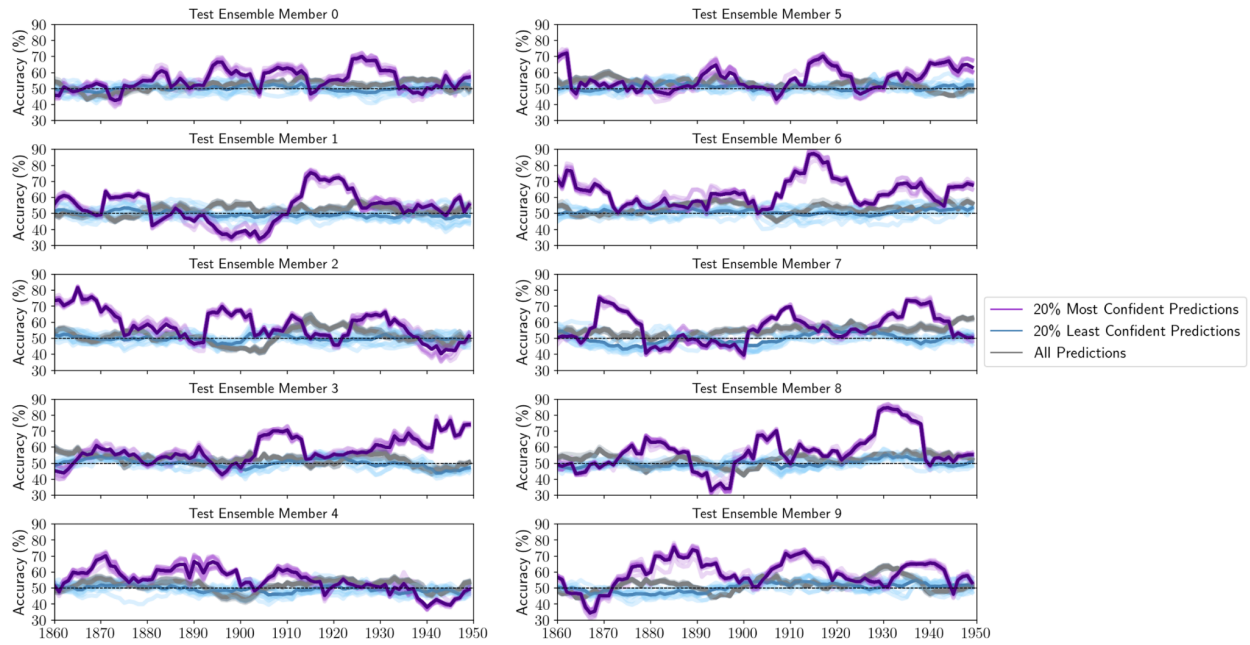


Supplemental Figure Figure S2. 10-year moving windows of accuracy shifted forward by 1 year for 10 random seeds of each of the 10 CESM2 test ensemble members for all predictions (gray), the 20% most confident predictions (purple), and the 20% least confident predictions (blue) for Alaska. Darker lines represent the average of the 10 random seeds.



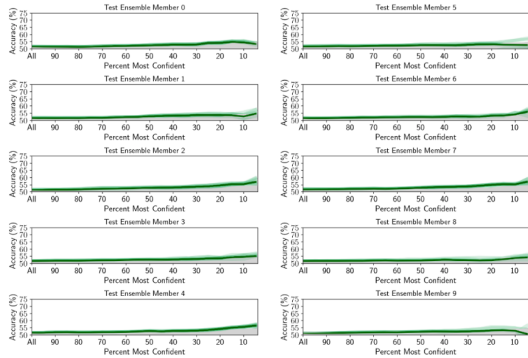
Supplemental Figure Figure S3. Same as Supplementary Figure S2 but for the Pacific Northwest.

### 10-yr Windows of Accuracy for Confident Predictions for CESM2 California

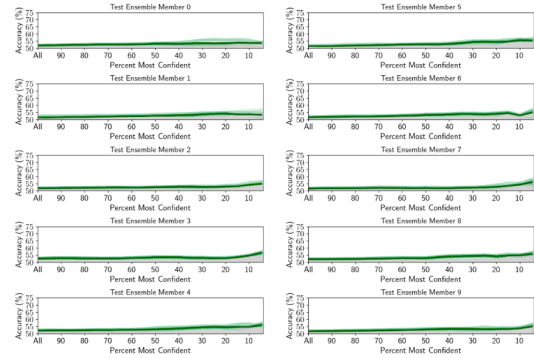


Supplemental Figure Figure S4. Same as Supplementary Figure S2 but for California.

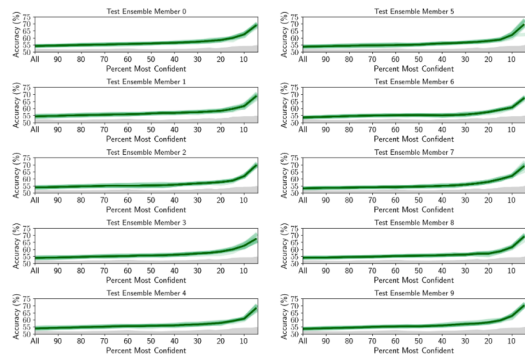
#### Model Prediction Accuracy for Various Confidence Thresholds for Alaska



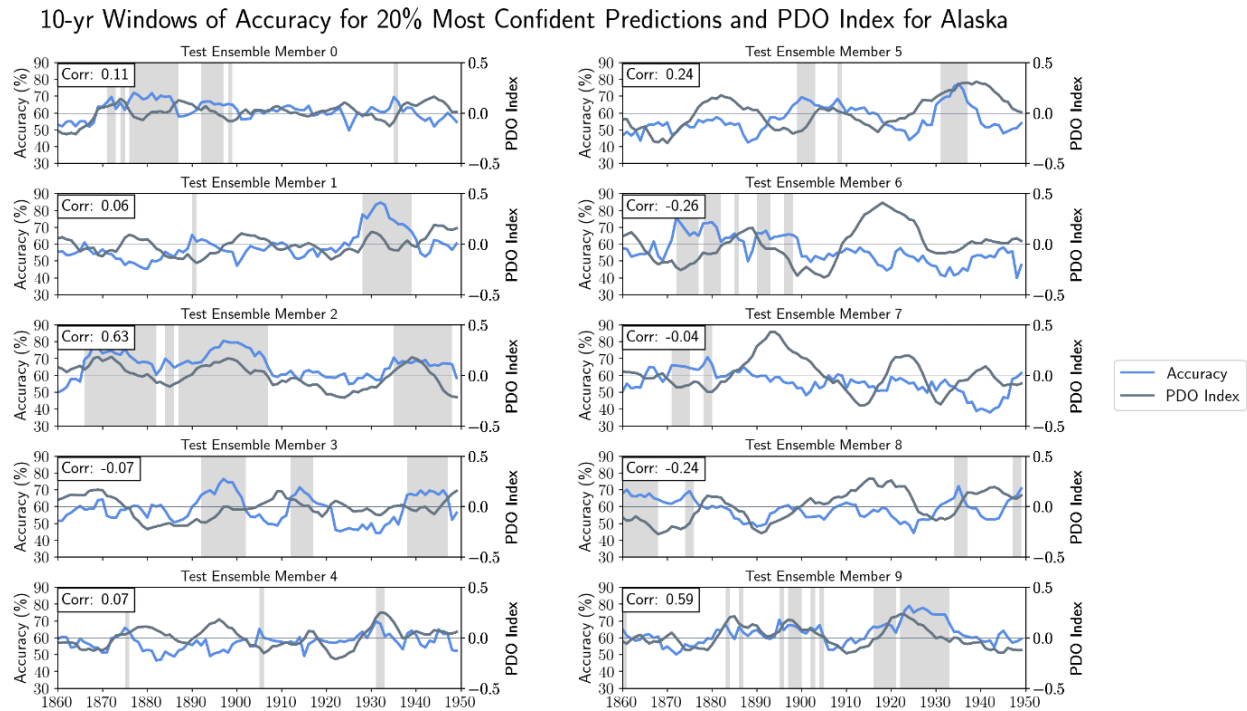
#### Model Prediction Accuracy for Various Confidence Thresholds for Pacific Northwest



#### Model Prediction Accuracy for Various Confidence Thresholds for California



Supplemental Figure S5. Accuracy versus confidence for all ten experiments using ERA5 data for a) Alaska, b) Pacific Northwest, and c) California. Green lines show the accuracy for the ERA5 testing data for ten random seeds for each experiment and dark green lines show the average of the random seeds.



Supplemental Figure S6. Blue lines show the 10-year moving window of accuracy shifted forward 1 year for the 20% most confident predictions for each of the 10 test ensemble members for Alaska. Gray lines show the PDO index calculated for each corresponding CESM2 ensemble member using the Program for Climate Model Diagnosis and Intercomparison (PCMDI) Metrics Package. Gray shading indicates accuracy over 65%. Upper left boxes show the correlation between the two timeseries.